Brandon Sargent
Department of Mechanical Engineering,
Brigham Young University,
Provo, UT 84602
e-mail: bsargent@byu.net

Jared Butler
Department of Mechanical Engineering,
Brigham Young University,
Provo, UT 84602
e-mail: jaredbutler@byu.net

Kendall Seymour
Department of Mechanical Engineering,
Brigham Young University,
Provo, UT 84602
e-mail: kennyseymour@byu.edu

David Bailey
Intuitive Surgical, Inc.,
Sunnyvale, CA 94086
e-mail: David.Bailey@intusurg.com

Brian Jensen
Department of Mechanical Engineering,
Brigham Young University,
Provo, UT 84602
e-mail: bdjensen@byu.edu

Spencer Magleby
Department of Mechanical Engineering,
Brigham Young University,
Provo, UT 84602
e-mail: magleby@byu.edu

Larry Howell[1]
Department of Mechanical Engineering,
Brigham Young University,
Provo, UT 84602
e-mail: lhowell@byu.edu

An Origami-Based Medical Support System to Mitigate Flexible Shaft Buckling

This paper presents the development of an origami-inspired support system (the OriGuide) that enables the insertion of flexible instruments using medical robots. Varying parameters of a triangulated cylindrical origami pattern were combined to create an effective highly compressible anti-buckling system that maintains a constant inner diameter for supporting an instrument and a constant outer diameter throughout actuation. The proposed origami pattern is composed of two repeated patterns: a bistable pattern to create support points to mitigate flexible shaft buckling and a monostable pattern to enable axial extension and compression of the support system. The origami-based portion of the device is combined with two rigid mounts for interfacing with the medical robot. The origami-based portion of the device is fabricated from a single sheet of polyethylene terephthalate. The length, outer diameter, and inner diameter that emerge from the fold pattern can be customized to accommodate various robot designs and flexible instrument geometries without increasing the part count. The support system also adds protection to the instrument from external contamination. [DOI: 10.1115/1.4045846]

Keywords: compliant mechanisms, folding and origami, medical robotics

1 Introduction

Robot-assisted surgery (RAS) is one of the fastest growing sectors in the medical device industry with robots taking over tasks originally performed by the operating staff, even to the point of becoming autonomous [1–5]. RAS can enable surgeons to use robotically driven instruments, such as endoscopes and catheters, with high precision. The long, thin, and flexible geometries of these instruments provide access to a large range of anatomies with little trauma on the patient. The instruments are also often outfitted with sensitive equipment such as biopsy tools, lights, or endoscopes. These traits create an instrument that provides many benefits but requires great care while handling *ex vivo* to prevent damage to the instrument. Traditionally inserted by hand, the proper handling of these instruments by surgeons is an ability not easily replaced but which medical robots are striving to provide.

While the instrument traits of length, flexibility, and size allow them to reach deep areas of the body, they generally cause the instrument to behave much like a rope or a cable, making them prone to buckling under *ex vivo* compressive insertion loads. This behavior complicates insertion since the instrument must undergo compressive loading to be inserted into the body, as shown in Fig. 1.

This work presents the fundamentals of an origami-based support system (the OriGuide) created to guide these flexible instruments *ex vivo* during RAS procedures. The OriGuide provides support points during insertion to mitigate shaft buckling and expanding sections to enable the extension and compression of the system through the integration of both monostable and bistable patterns into a single sheet. It shields the flexible instruments from contamination and provides a low-cost, low-part-count alternative to existing support devices.

1.1 Background.

This section provides a brief background on the use and importance of flexible instruments in RAS to provide context for the OriGuide's development. This is followed by a short discussion on origami-based design and how its benefits justify its use in this work.

1.1.1 Flexible Instrument Insertion. Medical robots are being designed for a variety of uses but have begun to take a large role in minimally invasive surgery (MIS) procedures [6,7]. MIS approaches are desirable due to the reduced trauma on the patient, leading to less pain and shorter post-operative healing times as

[1]Corresponding author.

Contributed by the Mechanisms and Robotics Committee of ASME for publication in the Journal of Mechanisms and Robotics. Manuscript received May 21, 2019; final manuscript received December 16, 2019; published online December 23, 2019. Assoc. Editor: Xianwen Kong.

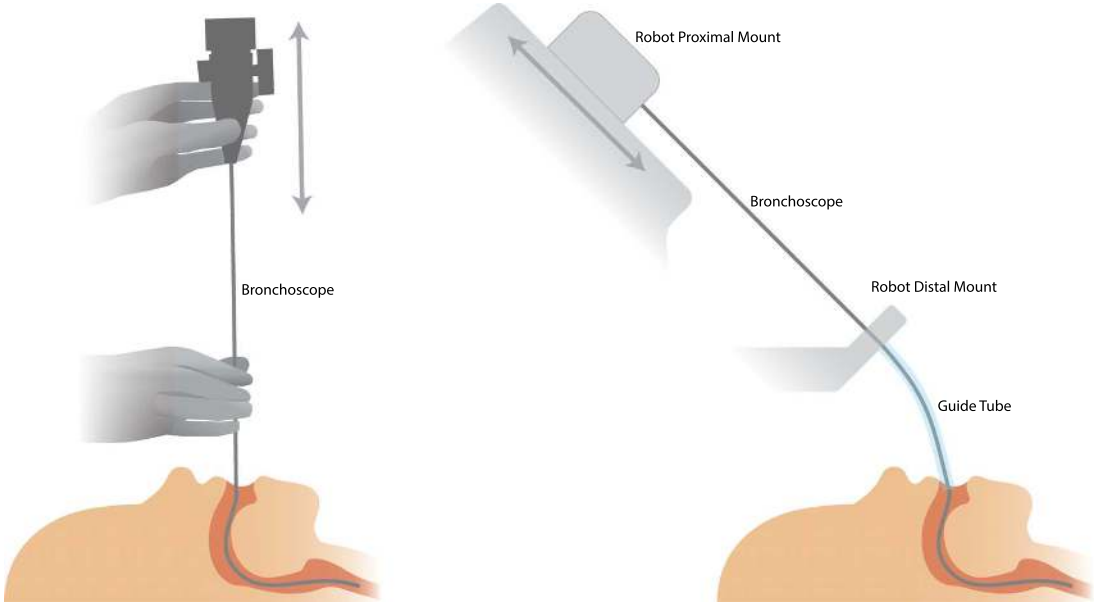

Fig. 1 Comparison of manual and robotic insertion of a bronchoscope. (*a*) A surgeon manually inserting a flexible instrument. (*b*) A medical robot inserting a flexible instrument.

well as improved cosmesis [8,9]. An essential part of an MIS approach is the size of the instruments used. MIS approaches are performed through one or more small incisions as opposed to an open approach with one large incision. The devices used to perform the surgery are inserted through the small incisions, typically accompanied by an endoscope to view the surgical space.

There are a number of MIS procedures that include flexible instrumentation [10–15] such as diagnosis of bronchial pathologies, spinal fusions, and removal of the spleen, appendix, or gall bladder [16–19]. Flexible instrumentation allows the surgeon to use the natural structure of the body, such as blood vessels, the gastrointestinal tract, or the airways, to guide the device to the desired area. The flexible devices also allow more versatility to the selection of the insertion location and may remove the need for an incision by enabling the use of natural orifices such as the nose or mouth as insertion points.

With manual insertion, a surgeon applies a compressive load on a section of the flexible instrument near the insertion site, which allows them to provide significant force to the instrument without risk of buckling. The surgeon simultaneously operates the control system for the instrument to guide it to the desired location (see Fig. 1(*a*)). The development of driven instruments has provided the ability for robotic assistance in these operations with the surgeon guiding the instrument from a control console. These driven instruments have a high degree of control and can be steered with greater accuracy than that of a passive, under-controlled instrument. Such robotically driven instruments are finding particular use in minimally invasive diagnosis and treatment of deeply remote anatomy that would be otherwise impossible to reach without more invasive methods. Driven instruments in RAS are predicted to enable more procedures in the future [20,21].

An example of one such procedure is a robotic bronchoscopy [22], which allows for real-time guiding through the lungs to view and take samples at pre-determined sites. Two methods are commonly used in manual lung biopsies, a transthoracic biopsy—a needle biopsy through the chest wall—and a transbronchial biopsy—a biopsy taken as part of a bronchoscopy. A needle biopsy provides access to deep areas of the lung but carries a risk for lung collapse when puncturing the lung wall [23]. This risk is lowered with a bronchoscopy as the biopsy is not taken through the lung wall but through the natural airways of the body. However, this access path limits the depth that the instrument can reach by the diameter of the instrument. Therefore, longer and thinner instruments may enable surgeons to choose more desirable access sites. Thinner instruments also decrease trauma caused by the instrument rubbing against the natural orifices of the body. In bronchoscopes, side effects caused by instrument rubbing are irritation of the airways (bronchospasm) or irritation of the vocal cords (laryngospasm). Smaller instruments can also allow for better air flow during the procedure [24]. However, thinning the instrument also increases its tendency to buckle and crease.

For robotic insertion of flexible instruments, the *ex vivo* support system is required to perform several tasks within the constraints of the robotic system. Foremost among these is the prevention of the buckling of the device. Current robotic insertion methods typically align the instrument in a straight line before insertion as this allows the robot to use shape-sensing technology [25,26], have constant access to the various cables and instrumentation attached at the proximal end of the flexible instrument, and avoid damage to the instrument. The flexible instrument is connected to this instrumentation at the proximal robot mount and the robot advances this mount toward the distal mount at the patient (Fig. 1(*b*)). Therefore, the support system must provide lateral support to the instrument from the proximal end to the insertion point into the patient. The support system should also help prevent external contaminates from attaching to the instrument to decrease the risk of infection [27,28].

1.1.2 Origami-Based Design. Any medical device used in the body must be either disposable or sterilizable for reuse. This sanitation requirement makes devices that are low-cost or easily sterilized appealing. The part count and complexity of a device is directly correlated with its cost and capacity to be sterilized, making devices that are created with minimal parts desirable. Devices fabricated from fewer pieces have increased potential to be disposable, are easier to clean, and can be less expensive to manufacture.

Origami offers opportunity to aide in reducing the part count in medical devices. Origami-based mechanisms are customizable, from their scale to the forces they output. They can be designed to be monolithic. Because origami is traditionally created from a single sheet, many origami-based mechanisms can be designed for planar manufacture in sheet materials, leading to lower production costs. Research into the unique behaviors achievable by origami

continues to expand our capacity to utilize this art form for engineering purposes [29–32]. Its unique motion has provided footing for the emergence of new mechanisms [33]. Analysis of origami and its motion has already found application in robotics [34–40] and has been used in the development of medical devices [41–43].

Traditional origami models are considered a class of mechanisms called compliant mechanisms, which are devices that gain some or all of their motion through deflection of elastic members rather than traditional hinges or bearings [44]. Compliant mechanism design can assist in reducing part count, increasing precision, and reducing manufacturing and assembly costs by replacing rigid links and joints with compliant mechanisms. Compliant mechanisms can also be designed from materials that are approved for use in medical devices and designed for harsh environments. They have been used in medical robotic systems design to reduce part count and size [45–47].

The principles of origami-based design and compliant mechanisms inspired the creation of the OriGuide. The OriGuide provides anti-buckling support with a low part count and new, enabling features to the robotic insertion system while providing support to the thin, flexible devices used in medical robotics.

1.2 Objectives. A well-designed flexible instrument support system should achieve the following objectives to ensure reliability, achieve positive patient outcomes, and make it robust and useful in varying applications.

1.2.1 Buckling Mitigation. The primary objective of the support system is to create a laterally stiff mechanism around the flexible instrument. This is quantified by the amount of deflection the mechanism undergoes under a lateral load. As the flexible instrument begins to buckle, it will deflect laterally against the support system at the interface points. The support system should be sufficiently stiff to restrict the deflection of the instrument under normal operating loads.

1.2.2 Motion. The support system should provide support through the continuous change in the *ex vivo* length of the instrument during the insertion process. This requires the laterally stiff support system to change length as the instrument is inserted (Fig. 2).

The support system should also have a large deployment ratio (ratio of the fully extended length to compressed length) to maximize the usable length of the instrument. The fully compressed length of the support system subtracts from usable instrument length because a segment of the instrument remains between the proximal and distal ends of the mounts when fully inserted (Fig. 2).

1.2.3 Force-Deflection. To maximize compatibility and control from the governing robot, the supporting system needs to have a predictable, repeatable compression and extension force response. This will enable the control system to easily accept the system as a part of its operation without large changes to the control programing. Primarily, the force response must be low to keep within the operating range of the robotic actuators. As the design of the device may be utilized for different robots, the force response would ideally be tailorable to match different force profiles required by different robots.

1.2.4 Tailorability. There are many designs and shapes of medical robots that may insert a flexible instrument into the body. A support system that protects and supports the flexible instrument during insertion should therefore be as customizable as possible, allowing the dimensions of the support system design to be easily altered to fit the dimensional constraints of a given robot. This may require a change in overall fully extended length, compressed length, and radial dimension measured laterally out from the flexible instrument (Fig. 2).

The support system may also be used for various procedures with different stroke lengths and instrument sizes, which would require a design tailorable to different dimensional requirements, specifically the inner diameter that interfaces with the instrument.

2 Methods

In this section, the design of the OriGuide, including the geometric and mechanical properties of the pattern, is discussed. Validation through physical testing is presented.

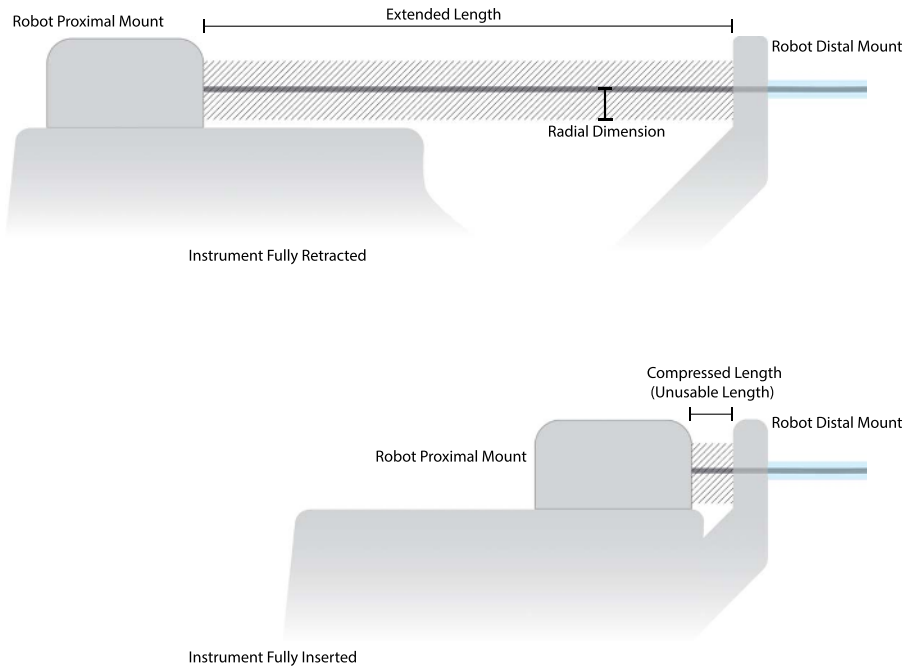

Fig. 2 A schematic of dimensional requirements associated with the robot and other geometry. The hatched section represents the area in which the support system must operate.

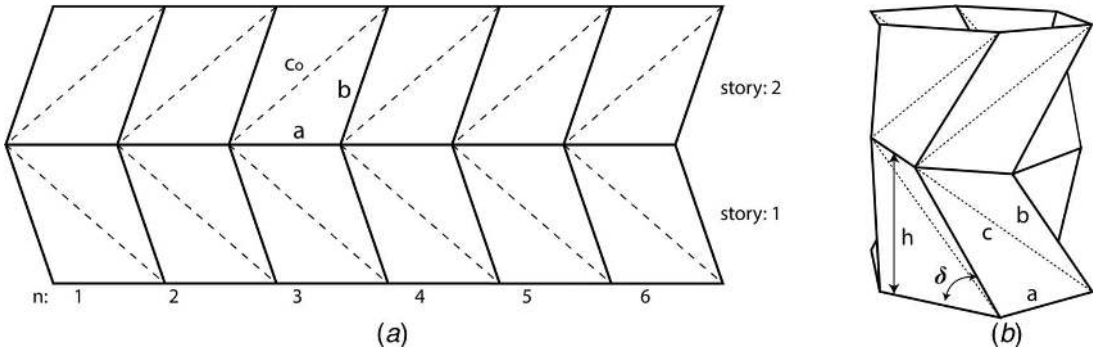

Fig. 3 A triangulated cylinder pattern with two stories and $n = 6$. The pattern is one fundamental component of the OriGuide. (*a*) Labeled flat pattern. (*b*) Pattern folded into a cylinder illustrating deployment angle and story height.

2.1 Triangulated Cylinder Origami Base Pattern. The OriGuide is composed of a series of primary origami mechanisms using a triangulated cylinder origami pattern [48–51]. Many patterns were analyzed as potential candidates, but due to several unique characteristics exhibited by this pattern, it was selected as the base to be modified and combined to achieve the properties unique to the OriGuide. Triangulated cylinder patterns have been used in various applications, including sunshields for space telescopes [52], bellows for martian spacecraft [53], and debris barriers for asteroid drilling [54]. The pattern is characterized by a series of tessellated triangles (Fig. 3(*a*) shows an example fold pattern). The triangle is mirrored along its largest length, c_o, to form a parallelogram. This unit is tessellated into a line of mirrored parallelograms and wrapped into a cylindrical pattern. The series of mirrored parallelograms, called a story, is stacked one upon each other to create the height of the cylinder. c_o is folded as a valley fold (shown as a dashed line in Figs. 3 and 4) while all other folds are mountain folds (solid lines a and b). The number of parallelograms tessellated in a story is the number of sides, n. Figure 3 shows an example of the pattern with two stories (one story mirrored) and $n = 6$ in the flat sheet pattern and then folded into a cylinder. Figure 4 shows the progression from a flat sheet to a folded, triangulated cylinder. The edge dimensions of a triangle in the pattern, a, b, and c_o, are defined by three variables: the outer diameter (D_o), folded-state inner diameter (D_i), and the number of tessellated sides in the pattern (n). These edge dimension relationships are discussed in Ref. [53] and are determined by

$$a = D_o \sin(\phi) \tag{1}$$

$$b = D_o \sin\left(\cos^{-1}\left(\frac{D_i}{D_o}\right) - \phi\right) \tag{2}$$

$$c_o = D_o \sin\left(\phi + \sin^{-1}\left(\frac{b}{D_o}\right)\right) \tag{3}$$

where

$$\phi = \frac{\pi}{n} \tag{4}$$

This triangulated cylinder compresses axially with a changing inner diameter and constant outer diameter (Figs. 5 and 6).

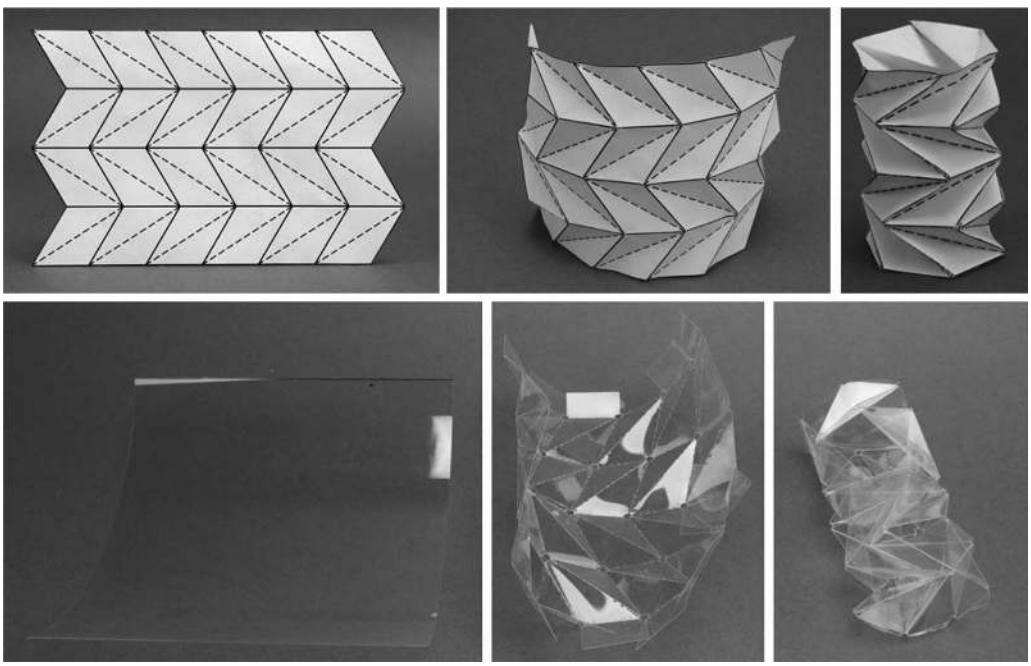

Fig. 4 Demonstration of pattern progressing from flat to folded in paper and PET. The device has four stories and $n = 6$.

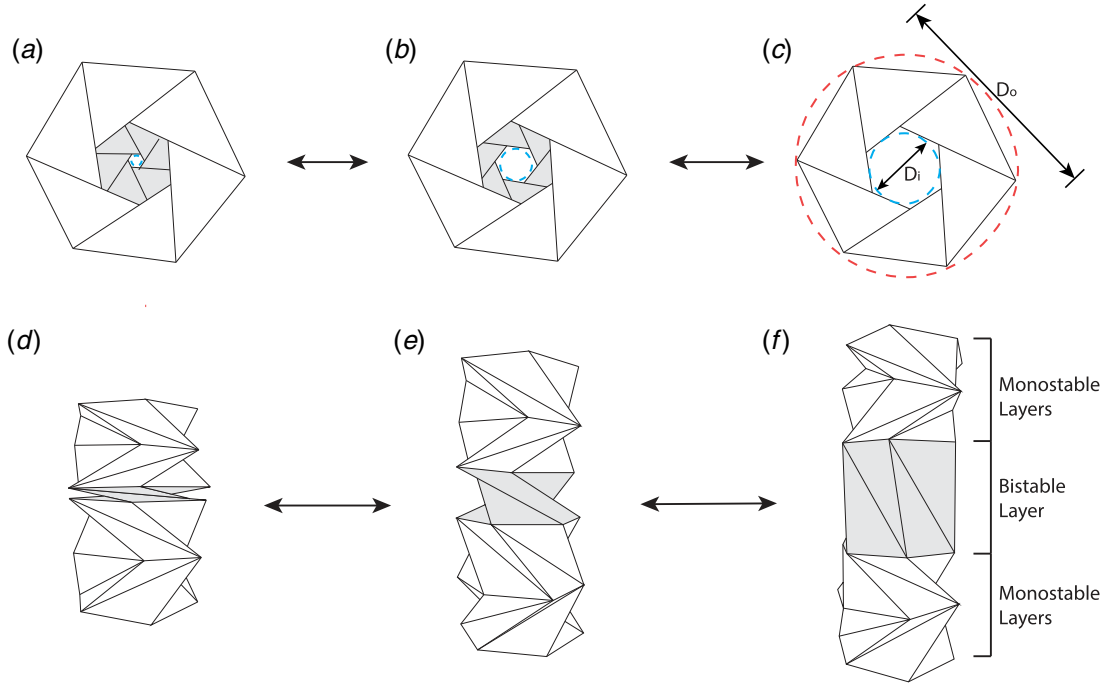

Fig. 5 Demonstration of top and side view of a five story pattern with $n = 6$, showing a constant D_o and changing D_i of the bistable layer as it is actuated from one stable state to another. The shaded story is designed to exhibit bistable behavior with positions A/D and C/F being the two stable points. The white layers are designed to exhibit monostable behavior. In the folded position (A/D), this layer provides a discrete support point with the D_i of the shaded story matching that of the instrument.

The panels formed by the triangles fold flat into the cross-sectional plane of the cylinder. This creates an inner diameter of the tube that decreases as the pattern is folded (see Figs. 5 and 6). The final, flat-folded inner diameter (D_i) is used to characterize the parameters of the pattern.

The parameters of the pattern can be tuned for the specific application, such as having a folded inner diameter that matches the diameter of a flexible device. The flexible device could then be fed through the center of the cylindrical mechanism and the pattern would provide discrete support points for the device. As support points are added along the device, the critical buckling load of the flexible device increases. The problem arises where the inner diameter of this pattern changes during actuation. The varying inner diameter of the triangulated cylinder is undesirable as it

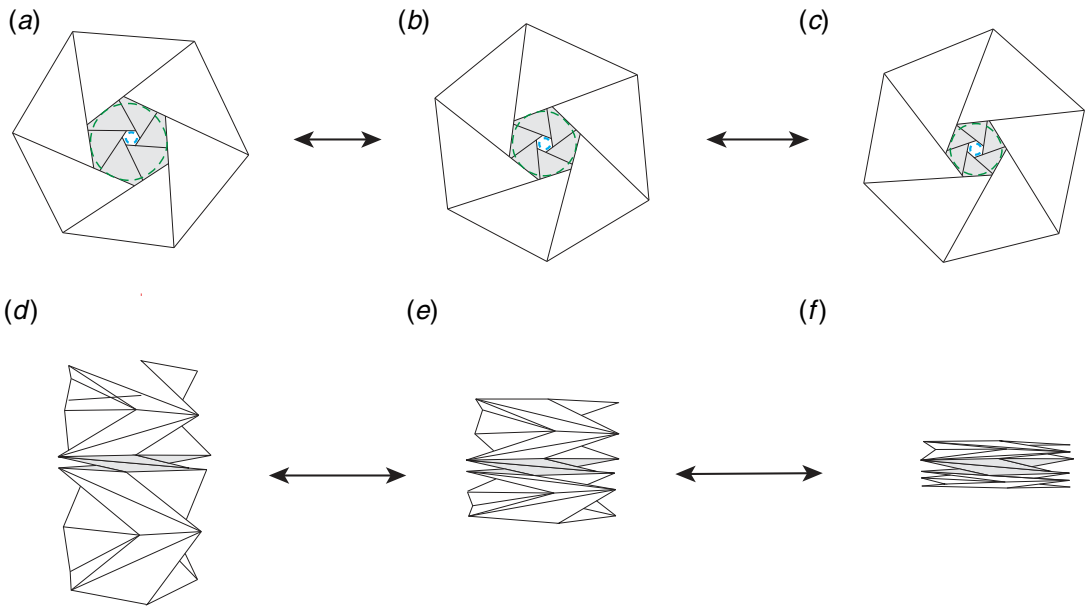

Fig. 6 Demonstration of top and side view of the same pattern as in Fig. 5, showing a constant D_i of the bistable layer and changing D_i of the actuation layers as it is actuated. This demonstrates the typical actuation of the OriGuide during use. The shaded bistable layer is designed to stay in the folded configuration through actuation, providing a constant D_i support point. The D_i of the white actuation layers changes slightly through actuation. The white layers are designed to have smooth actuation though the stroke.

would only provide adequate support points when the device is fully compressed. Further investigation of the pattern characteristics enabled the development of a novel pattern that resolves this issue.

The triangulated cylinder pattern is composed of multiple stories, where each story in the cylinder can be actuated independently. In this work, it was determined that for the same D_o and n, a different value of D_i can be selected for each individual story. This enabled the development of a highly customizable pattern with multiple inner diameters and actuating properties.

2.2 Bistability of the Triangulated Cylinder Pattern. It has been previously shown that the triangulated cylinder pattern can be made bistable [55,56], meaning a single story of the triangulated cylinder can be stable in two different positions along the actuation path. The OriGuide is an integration of monostable patterns to provide actuation and bistable patterns to provide support points (shown in gray in Figs. 5, 6, and 10). The bistable stories are stable in the closed, flat-folded position and the open position but are designed to remain in the closed position throughout the support system's actuation (position A/D in Fig. 5). They are tailored to have a folded inner diameter that matches the diameter of the flexible instrument. Therefore, these bistable layers become a series of discrete support points with unchanging inner diameters. The monostable stories were placed between the bistable layers and were designed to gain the maximum height per story during actuation while maintaining smooth actuation. This combination of bistable and monostable stories creates a single piece support system that maintains constant support points for the flexible instrument while allowing a change in length to enable the robot to insert the instrument into the body (Figs. 5 and 6).

The triangulated cylinder pattern can exhibit bistable behavior because it is not a rigid-foldable pattern [57], meaning it experiences strain and deformation in the creases and panels during actuation. The dimensions of the triangulated cylinder pattern can be tailored to provide a desired degree of stability, and strain energy curves can assist in determining when the pattern becomes bistable.

Simplified models have been developed to facilitate analysis of the strain in the pattern and [55,58] assumed that the majority of this strain occurs only in the creases. Strain was approximated as elongation in crease c_o only as a function of the deployment angle, δ, with the simplifying assumptions that a and b are completely rigid and that the pattern begins in a completely compressed state and actuates to a deployed state. The force–displacement relationship of a single unit cell of the triangulated cylinder pattern was examined [56] by studying the energy of the creases during actuation. Like Cai et al. [55,58], Yasuda et al. [56] simplified the model by removing the side facets and modeling the strain only in the creases. Lengths b and c_o were modeled as linear springs, and a as a fixed length.

These models identified patterns that exhibit bistable behavior when specific criteria are met. The model developed by Refs. [55,58] predicted bistability behavior for some patterns with $n = 6$, and Yasuda et al. [56] noted that the bistable behavior depended on the height of the deployed model. Bistability yields a stable position in both the deployed and stowed states. The dimensionless strain energy curve by Refs. [55,58] provides a way to mathematically predict if a pattern will be bistable under the assumption that deflection is only occurring in crease c_o. If the strain energy curve has a local maximum, then the corresponding pattern is bistable. If the strain energy curve has no local maximum, that pattern is monostable. The strain energy curves developed for varying pattern parameters are shown in Fig. 7.

Further work has been done as part of this study to verify the assumption that the majority of deflection occurs in crease c_o [59]. Using these assumptions, bistability can be predicted by the strain energy (w) where [55]

$$w(\delta) = \frac{1}{2}\left(\frac{c(\delta) - c_o}{c_o}\right)^2 \tag{5}$$

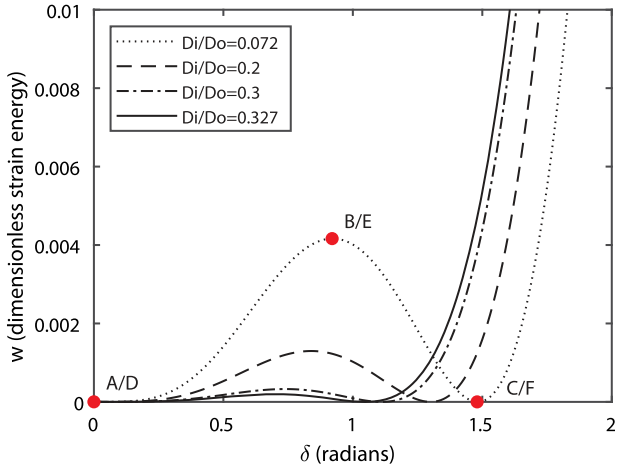

Fig. 7 Graphs showing various strain energy curves depending on the ratio of diameters for patterns with $n = 6$. Points highlighted correspond to the strain in the positions of the bistable story in Fig. 5. The solid line corresponds to the strain found in the monostable layers through actuation (Fig. 6).

and

$$c(\delta) = \sqrt{\left(D_o \sin\left(\phi + \sin^{-1}\left(\frac{b\cos(\delta)}{D_o}\right)\right)\right)^2 + (b\sin(\delta))^2} \tag{6}$$

The strain energy is a function of $c(\delta)$ (the changing length of c with respect to δ) and c_o (the flat folded value of c or $c(0)$), both of which are defined by the parameters D_o, D_i, n, and b. The length of b, as shown in Eq. (2), is governed by D_o, D_i, and n. Therefore, the design parameters of interest for determining the stability of a triangulated cylinder pattern are D_o, D_i, and n.

The diametric ratio is defined as the ratio of inner diameter to outer diameter. Varying the diametric ratio for a given n yields different stability behaviors. The diametric ratio at which the strain energy local maximum becomes zero is termed the stability transition ratio (STR) and represents the predicted transition point between monostable and bistable patterns for a given D_o and n. This predicted value is often lower than seen in physical prototypes due to the material properties, leading to a different practical STR value. Additional findings on how to predict the STR and design for bistable behavior can be found in Ref. [59].

Once a pattern of monostable and bistable layers has been developed, the relative motion of each layer can be predicted through the actuation stroke. If we consider each layer to act as a spring in series, the strain energy in each story should be equivalent throughout the stroke. δ for each layer determines both the strain energy in that layer through Eq. (5) and the deployed height of a given layer calculated as $b * \sin(\delta)$. Analogous to springs of similar stiffnesses in series, equivalent layers will have the same δ. To minimize strain in the system, the δ per layer type will be the largest while maintaining the lowest strain energy. Therefore, for a given point in the actuation stroke, the δ and stain energy for each layer can be found. If the strain in each layer were to exceeded the peak in the bistable strain energy (shown as point B/E in Fig. 7), the bistable layers will actuate quickly to the second, open configuration. Prior to this point, the bistable layers will actuate slightly, which will cause small changes in D_i at the support points. The support system is designed to operate in this range. For applications where no changes to D_i at the supports can be tolerated, the bistable layers can be adhered together in the closed position with adhesive.

2.3 Prototype Pattern Development. Consideration should be made for both general considerations and for constraints specific

to an application. This section discusses these considerations and constraints to create a successful support system.

Geometric constraints for a given application generally define D_o of the pattern, D_i for the bistable support layers, and the stroke length of the entire support. Maximizing the available D_o is beneficial in increasing height per story, ease of manufacturing, and designing for the bistable and actuation layers.

The STR is determined by n and D_o. Since D_o is usually maximized and constrained by the application, the choice of n determines the value of the STR. Larger values of n will increase the STR and allow for bistable layers with larger diameter instruments. However, an increase in n is also correlated with more complex manufacture due to the decrease in crease size and increase in crease number. Material properties also combine with the STR to determine the practical STR. More explanation on how to select the optimal n and determine the STR can be found in Ref. [59].

For the actuation layers, it is desirable to maximize the height of each layer. More stories in the device decrease the deployment ratio, resulting in more unusable flexible instrument length. Increasing the number of layers in the support system also increases the number of folds in the overall pattern, which increases parasitic motion, lowers the anti-buckling capabilities of the system, and complicates manufacture. As the length of side b is increased, the deployed height h of an individual layer increases at a given deployment angle δ. However, larger lengths of b for a given D_o also mean smaller diametric ratios, which could lead to a diametric ratio beneath the STR. Therefore, the STR serves as a check in finding the largest length b to maximize deployment height per story while maintaining monostability. As long as the diametric ratio of the actuation layers are above a practical STR, they will actuate smoothly. The number of actuation layers determines the fully extended length of the pattern through the number of actuation layers multiplied by $b * \sin(\delta)$ at full deployment. Modifying the number of stories or b of the actuation layers will provide for designing for a given fully extended stroke length.

Each actuation layer experiences rotation during actuation which would complicate interface of the device with the robot. This challenges of this behavior can be mitigated by using an even number of actuation layers with the number of stories rotating in one direction equivalent to the number of stories rotating in the other direction. This will result in zero rotation at both end mounts.

For the bistable layers, having a diametric ratio far below the STR will decrease motion in the layer through actuation. However, that motion is not zero, causing small fluctuations in the D_i of the support points. Depending on the application, this fluctuation could be significant. Adhesive can be added to the bistable layers, fixing them in the closed position. This ensures that actuation occurs only in the monostable layers and the D_i of the support points remains constant through the stroke. The bistable layers play little in overall extended length but do have a significant effect on the compressed length. For maximum support, bistable layers can be placed between every actuation layer. While this increases the support points, it will also cause rotation of bistable layers positioned between mirrored actuation layers. This may result in undesired motion of the supported flexible instrument. When possible, it is recommended that an even number of mirrored sets of actuation layers are on either side of each bistable support layer to remove the rotation. An even number of bistable layers, each mirrored from the previous, will ensure that the profile at the mounts is at the same angle.

The highest strain in the support system occurs at the vertices [59]. Small holes can be cut at the vertices to avoid failure at these points. By removing the vertices, the axial force to actuate, strain in the panels, and noise during actuation are reduced. However, creating these holes does slightly reduce the amount of shielding provided by the support system from external contamination.

Various sheet materials can be chosen based on their folding properties. Primarily analyzed in this work is polyethylene terephthalate (PET), the same plastic found in common recyclable water bottles. This material is recommended for its properties of high tensile strength, formability under heat, recyclability, and biocompatibility. This material also is a semi-crystalline material that can be treated through heat setting. This treatment is used to change the crystallinity, creating a lowest energy state at a given folded position. Biasing the lowest energy state to occur in the compressed state allows the support system to remain in tension during use. Because buckling is primarily compressive failure mode, a support system that is always in tension is free from the risk of buckling. This is an important feature as the initial folded state is long and highly prone to buckling as can be seen in Fig. 8(*a*). By changing the natural state to that in Fig. 8(*b*), the support structure will not bend or buckle under linear actuation loads. The additional tension also makes the system more laterally stiff through stress stiffening, creating a more effective support structure for the flexible device. The development and study of the heat setting process used here, as well as findings on the fundamentals of using a heat set in PET for origami mechanisms, can be found in Ref. [60] and can be used to tailor the force response of the support system.

The origami-based portion of the support system is created within the single sheet of foldable material, allowing for customization without a change in part count. Rigid mounts are added to connect the origami mechanism to the robot, resulting in a support system of only three parts, shown in Fig. 9. Slots were made for inserting end tabs added to the pattern and the tabs were adhered into the slots. Supporting tabs were added to the mounts for added stability. The support tabs interlock when the pattern is fully compressed and has a length equal to the compressed length to ensure the supporting tabs do not add to the compressed length.

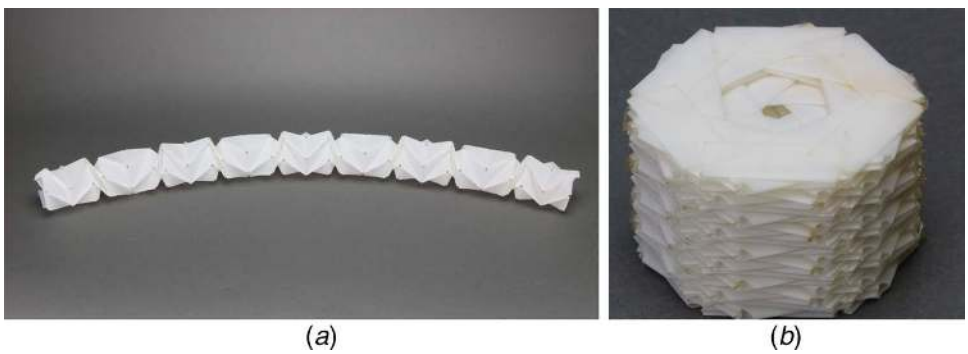

Fig. 8 Matte PET OriGuide component in various stages of manufacture. By using a heat set to transfer the support structure from its initial configuration (*a*) to a natural state in the compressed state, (*b*) the support structure will be in extension throughout the stroke and therefore not bend or buckle under normal actuation loads. (*a*) Folded pattern before heat set. (*b*) Folded pattern after heat set.

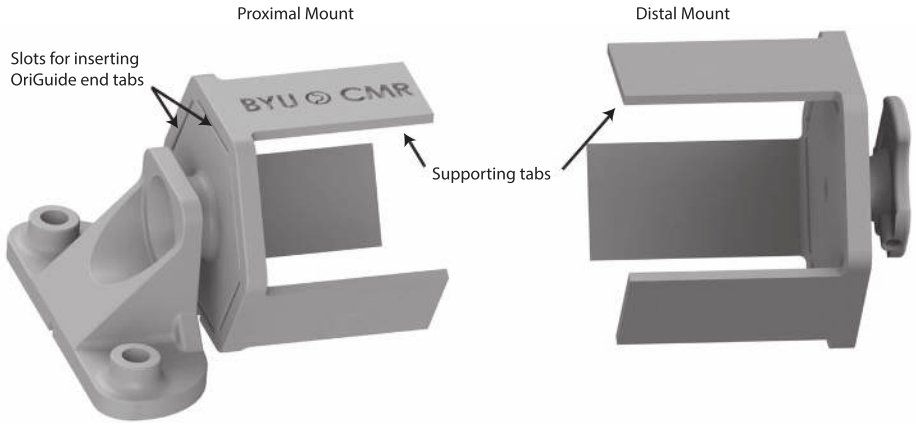

Fig. 9 Computer aided design rendering of proximal and distal mounts. Support tabs added stability without increasing compressed length. Geometry was made to interface with a current robotic system.

2.4 Testing. With a general approach defined, a prototype was designed to support an endoscope for use on a bronchoscopy surgical robot.

2.4.1 Prototype. To create a full anti-buckling support system, eight bistable stories were combined with 18 monostable stories in an alternating order. The parameters used in the prototype tested can be found in Table 1 and a scaled copy of the pattern is shown in Fig. 10. The bistable layers, when collapsed, create an inner diameter of 4 mm. The total device length when extended is just over 500 mm and can be compressed to just under 50 mm.

For the full stroke of 500 mm, the number of monostable layers was chosen to ensure that bistable layers remained far from the strain energy required to transition to the open configuration. At maximum extension per layer, δ of the monostable layers was designed to be just under 1 radian. The equivalent maximum strain per layer predicted the displacement of the bistable layers to be approximately 0.27 radians. This would make the bistable layers actuate to increase D_i from 4 to approximately 6.8 mm. To ensure this small deflection does not occur, adhesive was added for additional stability in the closed position. Therefore, no motion was observed in the bistable layers and the D_i of the support points remained at 4 mm through the entire stroke.

The sheet material used for the support system is 0.13 mm (0.005 in.) thick PET sheet. The chosen fold pattern was first scored into the PET sheet using an Epilog Fusion M2 laser cutter. The laser cutter was run with conservative settings (3% power and 50% speed) to score the pattern into the PET and slightly higher settings (8% power and 50% speed) to cut. The cut and scored pattern was folded by hand and adhere into the proper tube shape, using strips of 0.051 mm (0.002 in.) PET coated with an acrylic-adhesive. The bistable layers were collapsed to their compressed state and the entire model was heat set. The bistable layers were afterward adhered closed using a small amount of Loctite 4981 adhesive to add stability in the closed position. The same adhesive was used to attach the full pattern to the mounts.

For the heat set, the pattern was compressed to 40 mm in length and heated in an oven at 150 °C for 90 min, followed by a period of slow cooling. The sample was left compressed in the oven while the oven was turned off and allowed to slowly cool to room temperature. The pattern before and after heat setting can be seen in Fig. 8.

For this prototype, holes were elected to be cut in the vertices to reduce noise in actuation, lower actuation force, and reduce the chance of local failure. Figures 8 and 11–13 show samples of the support system manufactured using clear, colored, matte, and reflective, metallic-backed PET before heat setting. These samples showed that the system can be made in various types of stock PET sheets.

2.4.2 Testing Methods. Comparative testing was done to assess the effectiveness of the support system compared to using no external supports. A custom sliding arm fixture was constructed to test the buckling resistance of each prototype (Fig. 14). It includes

Table 1 Parameters for the physical model

	a (mm)	b (mm)	c (mm)	n	Material	Thickness (mm)
Actuation layers	27.5	36.01	51.97	6	PET	0.13 ± 0.01
Support layers	27.5	45.51	55.83	6	PET	0.13 ± 0.01
Adhesive film					PET/Acrylic Adhesive	0.051 ± 0.005

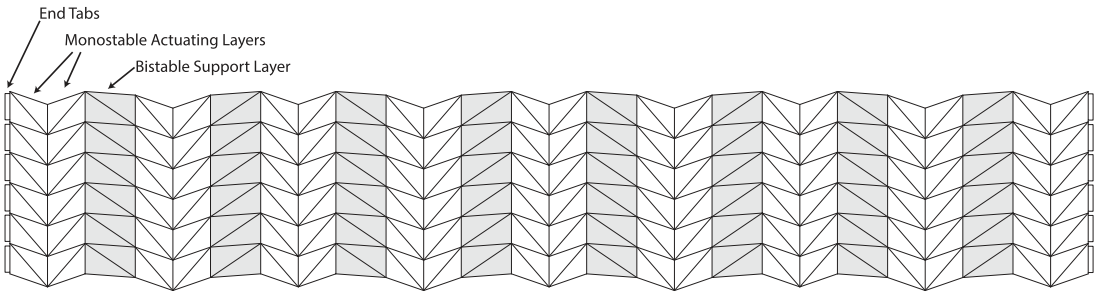

Fig. 10 To-scale version of the pattern used for the full system with the bistable support layers highlighted. Holes were cut at the vertices after the pattern was scored.

Fig. 11 Pattern demonstrated in matte, colored, and reflective, metallic-backed PET

a rigid distal mount and a sliding proximal mount compatible with a research robot developed by Intuitive Surgical, Inc., allowing the prototype support system to actuate in a controlled manner while supporting a flexible device. The support system was loaded with a 4 mm diameter endoscopic catheter and actuated to positions 5 cm apart.

Two tests were performed, representing static and dynamic loading conditions. The static test was performed by fixing the support system at a given length. The endoscope was loaded with an axial compressive load with a force sensor until failure. Failure occurred when the flexible device buckled, classified as supporting no additional compressive load, or the device began to plastically deform due to the compressive loads. The maximum force sustained before failure for the given length was recorded. This was repeated along a set of lengths from 0 cm to 40 cm in increments of 5 cm. Lengths were measured relative to the fully compressed, or fully inserted, position. This test evaluated the change in the critical buckling load, P_{crit}, of the flexible device. The endoscope was occasionally changed between prototype tests to ensure possible damage to the instrument did not effect future results. This test isolates the flexible instrument and helps determine the increase in buckling resistance of the instrument provided by the support system.

The dynamic test was performed on the custom sliding arm fixture by starting the sliding arm at a given length. The same endoscope was fixed at the proximal mount and the sliding arm was advanced from the starting length. The distal end of the device pushed on the force sensor until failure as measured in the static test. The force applied to the device as the system advanced was measured, and the peak force before failure was recorded as the dynamic critical load for the given starting length. The set of starting lengths was the same as the set used in the static test. This tests the system as a whole and includes the buckling resistance of the support system and instrument collectively.

For each test, the load was measured as an average force reading from the sensor over the course of approximately 1 s at the given applied load or position. This average was calculated and generated by the LabQuest digital readout used. A single value was recorded at each position. The error of the force sensor was ±0.01 N.

2.4.3 Results. The results of the static test can be found in Fig. 15(*a*). No results were given for lengths under 20 cm as the catheter failed in compression rather than buckling. For the

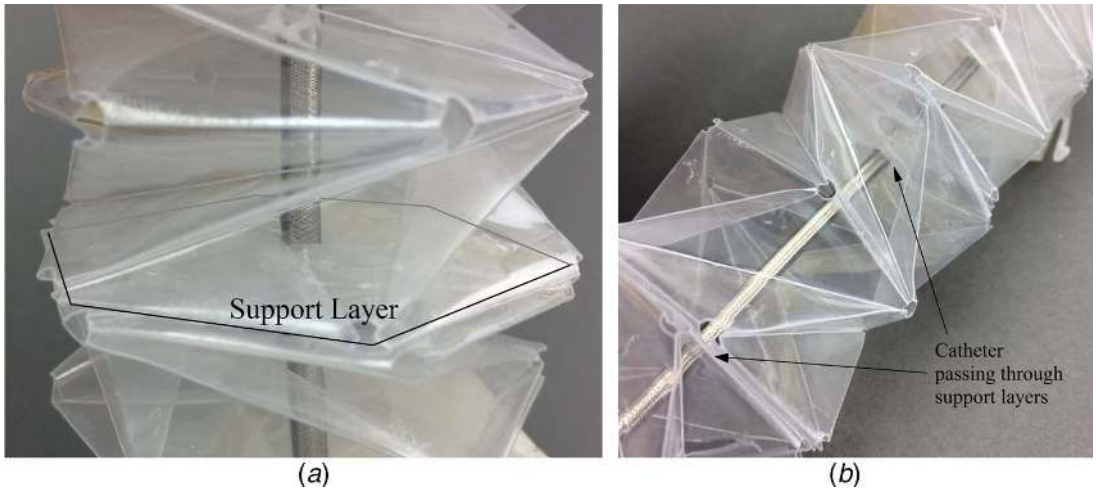

Fig. 12 Close up of clear PET OriGuide supporting an example instrument. (*a*) Instrument with single support layer marked. (*b*) Instrument passing though multiple support layers.

Fig. 13 Metallic-backed PET OriGuide. (*a*) Extended and (*b*) compressed.

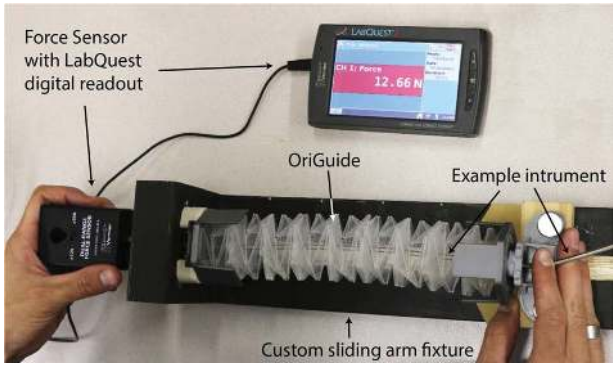

Fig. 14 Demonstration of the test setup

unsupported catheter, a value above 15 cm could not be determined because it did not support any significant load before buckling. The dynamic critical loads for a given starting position for both support systems are shown in Fig. 15(*b*). The catheter failed in compression rather than buckling for lengths under 0.1 m.

Figures 15(*a*) and 15(*b*) are shown with the unsupported endoscopic catheter buckling results. The instrument was tested at various lengths using a vertically mounted fixed-fixed condition (Instron tensile tester, load cell resolution ±0.125 N). The instrument began to buckle under its own weight at lengths above 0.15 m, resulting in effectively zero buckling strength. To help visualize the comparison to the OriGuide results, a power rule fit trend is extrapolated through the range of lengths tested.

The device was also demonstrated on a proprietary research medical robot developed by Intuitive Surgical, Inc. The OriGuide interfaced with the robot and successfully performed the task of preventing instrument buckling while actuating through the specified length.

3 Discussion

Figures 15(*a*) and 15(*b*) illustrate the effectiveness of the OriGuide in increasing the buckling strength of the example instrument. The dynamic test, which models how the system would be used in a medical application, shows an increase of 10 N or greater in buckling strength in the example instrument at every position when compared with the unsupported endoscope. A relative constant value about 15 N was held for the majority of the range. A sharp decrease was seen in both tests at large ranges of extension as the instrument buckled inside the support system between support points. At full extension, the support layers were about 60 mm apart. The power rule fit model of the unsupported catheter predicted about 10 N critical buckling load at 60 mm which agrees with the OriGuide results nearing full extension. If greater support is needed, additional bistable stories could be added between each pair of monostable stories. While this would decrease the compression ratio and leave more flexible instrument length unusable, it would reduce the length between support layers, resulting in increased buckling strength.

A fundamental physical phenomena behind the support system is the tension introduced into the system to support the flexible device and resist lateral forces as it begins to buckle. Therefore, a limitation of this design is the stiffness of the support system during actuation. This tensile force preload is added to the force of the robot inserting the flexible device, but it would also require a non-trivial amount of power from the robot to re-extend the support system after insertion. The heat setting process developed was designed to help engineers tailor the force response of their device through changing the parameters of the heating process.

One option for high-volume manufacturing of the support system involves using a rolling mill approach, where the desired pattern, including mountain and valley folds, could be machined into a roller. This could press the pattern onto a single sheet of material and pre-bias the folds. The seams in the pattern could then be laser-welded together and the pattern manually compressed, including collapsing and adhering the bi-stable layers and attached to a mounting fixture. The system could then be heat set, introducing the tension required in the system to mitigate buckling.

A second option for manufacturing involves laser-scoring the desired pattern into a thin sheet material. A die, with the proper mountain and valley pattern machined or formed into it, could be used to pre-bias each fold in the pattern. The seams would be laser-welded to form the creased sheet into a tube, which would then be compressed, the bistable layers adhered, and the ends attached to mounting fixtures. Heat setting could then be performed to keep the model in a specific state if desired.

The principles that enable the OriGuide have potential for use in applications beyond medical robotics. The combination of monostable and bistable stories used for support and extension can be applied to other origami devices, such as those used in space and flexible electronics.

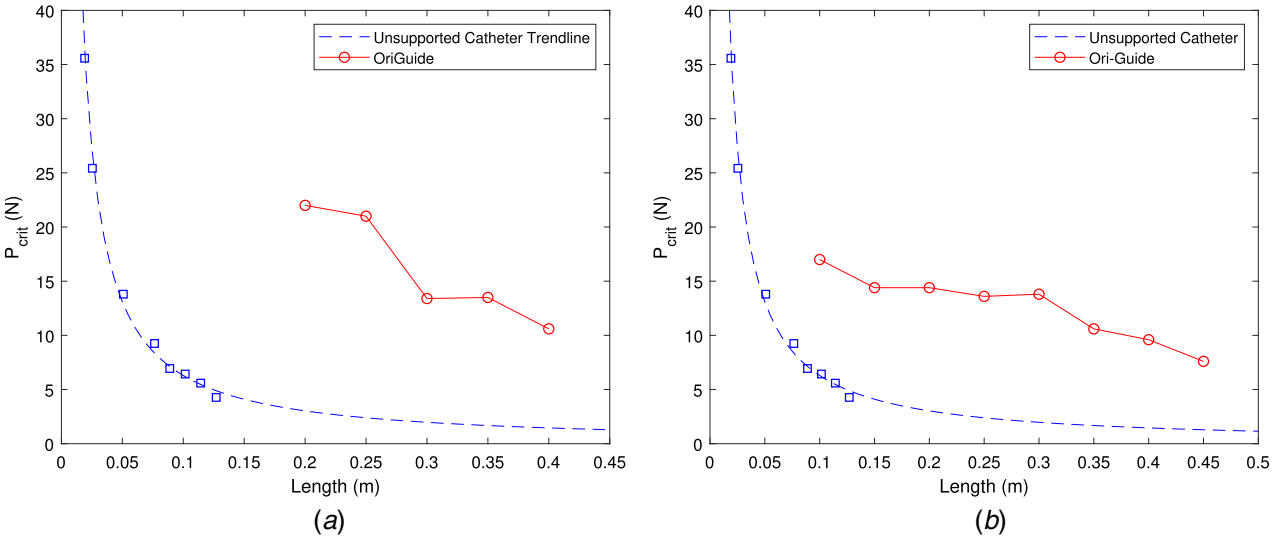

Fig. 15 Test results comparing the critical buckling load at given lengths in static and dynamic tests to the unsupported catheter critical buckling load. The resolution of the testing was ±0.01 N for the OriGuide tests and ±0.125 N for the unsupported catheter tests. (*a*) Static test and (*b*) dynamic test.

3.1 Conclusions. The OriGuide anti-buckling support system is capable of mitigating buckling in a flexible endoscope device. Varying parameters of a triangulated cylindrical origami pattern were combined to create an anti-buckling system with large compressibility that has a constant inner diameter for supporting a device and a constant outer diameter throughout actuation. The origami-based system has a low part count (3), which remains unchanged when the geometry is adjusted for different applications, including modifying the length, outer diameter, and inner diameter. The resulting pattern can be customized to fit various robot designs to work with long, flexible instruments. The design of the support system protects the flexible instrument from external contamination. Testing demonstrated that the OriGuide is an effective system for increasing the buckling support for insertion of a flexible instrument. The OriGuide can enable the use of longer and thinner instruments, improving the ability the surgeons have to access deep areas of the body and improve patient outcomes.

Acknowledgment

The authors would like to thank Janette Herron for her work and consultation on the selection and analysis of pattern dimensions. This paper is based on work supported by the U.S. National Science Foundation and the U.S. Air Force Office of Scientific Research through NSF Grant No. EFRIODISSEI-1240417, by NSF Grant No. 1663345, and by Intuitive Surgical, Inc.

References

[1] Diana, M., and Marescaux, J., 2015, "Robotic Surgery," Br. J. Surg., **102**(2), pp. 169–176.
[2] Shademan, A., Decker, R. S., Opfermann, J. D., Leonard, S., Krieger, A., and Kim, P. C., 2016, "Supervised Autonomous Robotic Soft Tissue Surgery," Sci. Transl. Med., **8**(337), p. 337ra64.
[3] Payne, C. J., Wamala, I., Bautista-Salinas, D., Saeed, M., Van Story, D., Thalhofer, T., Horvath, M. A., Abah, C., Pedro, J., Walsh, C. J., and Vasilyev, N. V., 2017, "Soft Robotic Ventricular Assist Device With Septal Bracing for Therapy of Heart Failure," Sci. Rob., **2**(12), p. eaan6736.
[4] Yang, G.-Z., Cambias, J., Cleary, K., Daimler, E., Drake, J., Dupont, P. E., Hata, N., Kazanzides, P., Martel, S., and Patel, R. V., Santos, V. J., and Taylor, R. H., 2017, "Medical Robotics-Regulatory, Ethical, and Legal Considerations for Increasing Levels of Autonomy," Sci. Rob., **2**(4), p. eaam8638.
[5] Lanfranco, A. R., Castellanos, A. E., Desai, J. P., and Meyers, W. C., 2004, "Robotic Surgery: A Current Perspective," Ann. Surg., **239**(1), p. 14.
[6] Liu, H., Lawrie, T. A., Lu, D., Song, H., Wang, L., and Shi, G., 2014, "Robot-Assisted Surgery in Gynaecology," Cochrane Database of Systematic Reviews, **12**.
[7] Mack, M. J., 2001, "Minimally Invasive and Robotic Surgery," JAMA, **285**(5), pp. 568–572.
[8] Jaffray, B., 2005, "Minimally Invasive Surgery," Arch. Dis. Child., **90**(5), pp. 537–542.
[9] Robinson, T., and Stiegmann, G., 2004, "Minimally Invasive Surgery," Endoscopy, **36**(1), pp. 48–51.
[10] Kyle M. Hatten, M., and Alexander Lin, M., 2017, "Transoral Robotic Surgery-Assisted Endoscopy With Primary Site Detection and Treatment in Occult Mucosal Primaries," JAMA Otolaryngol. Head Neck Surg., **143**(3), pp. 267–273.
[11] Yeung, A. T., 2017, "Robotics in the MIS Spine Surgery Arena: A New Role to Advance the Adoption of Endoscopic Surgery as the Least Invasive Spine Surgery Procedure," J. Spine, **6**(3), p. 2.
[12] Al-Ahmad, A., Grossman, J. D., and Wang, P. J., 2005, "Early Experience With a Computerized Robotically Controlled Catheter System," J. Interv. Card. Electrophysiol., **12**(3), pp. 199–202.
[13] Kanagaratnam, P., Koa-Wing, M., Wallace, D. T., Goldenberg, A. S., Peters, N. S., and Davies, D. W., 2008, "Experience of Robotic Catheter Ablation in Humans Using a Novel Remotely Steerable Catheter Sheath," J. Interv. Card. Electrophysiol., **21**(1), pp. 19–26.
[14] Jayender, J., Azizian, M., and Patel, R. V., 2008, "Autonomous Image-Guided Robot-Assisted Active Catheter Insertion," IEEE Trans. Rob., **24**(4), pp. 858–871.
[15] Li, Z., Oo, M. Z., Nalam, V., Thang, V. D., Ren, H., Kofidis, T., and Yu, H., 2016, "Design of a Novel Flexible Endoscopecardioscope," ASME J. Mech. Rob., **8**(5), p. 051014.
[16] Roza, M. A. D., Quah, K. H., Tay, C. K., Toh, W., Li, H., Kalyanasundaram, G., and Anantham, D., 2016, "Diagnosis of Peripheral Lung Lesions Via Conventional Flexible Bronchoscopy With Multiplanar CT Planning," Pulm. Med., **2016**, pp. 1–7.
[17] Kantsevoy, S. V., Hu, B., Jagannath, S. B., Vaughn, C. A., Beitler, D. M., Chung, S. S. C., Cotton, P. B., Gostout, C. J., Hawes, R. H., Pasricha, P. J., Magee, C. A., Pipitone, L. J., Talamini, M. A., and Kalloo, A. N., 2006, "Transgastric Endoscopic Splenectomy," Surg. Endosc. Other Interv. Tech., **20**(3), pp. 522–525.
[18] Yin, X., Guo, S., Xiao, N., Tamiya, T., Hirata, H., and Ishihara, H., 2016, "Safety Operation Consciousness Realization of a MR Fluids-Based Novel Haptic Interface for Teleoperated Catheter Minimally Invasive Neurosurgery," IEEE/ASME Trans. Mechatron., **21**(2), pp. 1043–1054.
[19] Roche, E. T., Fabozzo, A., Lee, Y., Polygerinos, P., Friehs, I., Schuster, L., Whyte, W., Berazaluce, A. M. C., Bueno, A., Lang, N., Pereira, M. J., Feins, E., Wasserman, S., O'Cearbhaill, E. D., Vasilyev, N. V., Mooney, D. J., Karp, J. M., Del Nido, P. J., and Walsh, C. J., 2015, "A Light-Reflecting Balloon Catheter for Atraumatic Tissue Defect Repair," Sci. Transl. Med., **7**(306), p. 306ra149.
[20] Camarillo, D. B., Krummel, T. M., and Salisbury, J. K., 2004, "Robotic Technology in Surgery: Past, Present, and Future," Am. J. Surg., **188**(4), pp. 2–15.
[21] Wang, H., Kong, D., and Zuo, S., 2019, "A Miniature Robotic-Assisted Tool for Large Area Endomicroscopy Scanning," ASME J. Mech. Rob., pp. 1–22.
[22] Fielding, D., Bashirzadeh, F., Son, J. H., Todman, M., Tan, H., Chin, A., Steinke, K., and Windsor, M., 2017, "First Human Use of a New Robotic-Assisted Navigation System for Small Peripheral Pulmonarynodules Demonstrates Good Safety Profile and High Diagnostic Yield Fielding," Am. Coll. Chest Phys., **152**(4), p. A858.
[23] Khan, M., Straub, R., Moghaddam, S., Maataoui, A., Gurung, J., Wagner, T., Ackermann, H., Thalhammer, A., Vogl, T., and Jacobi, V., 2008, "Variables Affecting the Risk of Pneumothorax and Intrapulmonal Hemorrhage in CT-Guided Transthoracic Biopsy," Eur. Radiol., **18**(7), pp. 1356–1363.
[24] Ricou, B., Grandin, S., Nicod, L., Thorens, J.-B., and Suter, P. M., 1995, "Adult and Paediatric Size Bronchoscopes for Bronchoalveolar Lavage in Mechanically Ventilated Patients: Yield and Side Effects," Thorax, **50**(3), pp. 290–293.
[25] Larkin, D. Q., and Shafer, D. C., 2011, "Robotic Surgery System Including Position Sensors Using Fiber Bragg Gratings," Apr. 19, U.S. Patent No. 7,930,065.
[26] Moore, J. P., and Rogge, M. D., 2012, "Shape Sensing Using Multi-Core Fiber Optic Cable and Parametric Curve Solutions," Opt. Express, **20**(3), pp. 2967–2973.
[27] Smith, R. S., Zhang, Z., Bouchard, M., Li, J., Lapp, H. S., Brotske, G. R., Lucchino, D. L., Weaver, D., Roth, L. A., Coury, A., Biggerstaff, J., Sukavaneshvar, S., Langer, R., and Loose, C., 2012, "Vascular Catheters With a Nonleaching Poly-Sulfobetaine Surface Modification Reduce Thrombus Formation and Microbial Attachment," Sci. Transl. Med., **4**(153), p. 153ra132.
[28] Raad, I. I., Hohn, D. C., Gilbreath, B. J., Suleiman, N., Hill, L. A., Bruso, P. A., Marts, K., Mansfield, P. F., and Bodey, G. P., 1994, "Prevention of Central Venous Catheter-Related Infections by Using Maximal Sterile Barrier Precautions During Insertion," Infect. Control Hosp. Epidemiol., **15**(4), pp. 231–238.
[29] DeFigueiredo, B. P., Pehrson, N. A., Tolman, K. A., Crampton, E., Magleby, S. P., and Howell, L. L., 2019, "Origami-Based Design of Conceal-and-Reveal Systems," ASME J. Mech. Rob., **11**(2), p. 020904.
[30] Feng, H., Peng, R., Ma, J., and Chen, Y., 2018, "Rigid Foldability of Generalized Triangle Twist Origami Pattern and Its Derived 6r Linkages," ASME J. Mech. Rob., **10**(5), p. 051003.
[31] Zhang, H., Zhu, B., and Zhang, X., 2019, "Origami Kaleidocycle-Inspired Symmetric Multistable Compliant Mechanisms," ASME J. Mech. Rob., **11**(1), p. 011009.
[32] Cai, J., Zhang, Q., Feng, J., and Xu, Y., 2019, "Modeling and Kinematic Path Selection of Retractable Kirigami Roof Structures," Comp. Aided Civil Infrastruct. Eng., **34**(4), pp. 352–363.
[33] Nelson, T. G., Zimmerman, T. K., Magleby, S. P., Lang, R. J., and Howell, L. L., 2019, "Developable Mechanisms on Developable Surfaces," Sci. Rob., **4**(27), p. eaau5171.
[34] Rafsanjani, A., Zhang, Y., Liu, B., Rubinstein, S. M., and Bertoldi, K., 2018, "Kirigami Skins Make a Simple Soft Actuator Crawl," Sci. Rob., **3**(15), p. eaar7555.
[35] Sung, C., and Rus, D., 2015, "Foldable Joints for Foldable Robots," ASME J. Mech. Rob., **7**(2), p. 021012.
[36] Sareh, P., Chermprayong, P., Emmanuelli, M., Nadeem, H., and Kovac, M., 2018, "Rotorigami: A Rotary Origami Protective System for Robotic Rotorcraft," Sci. Rob., **3**(22), p. eaah5228.
[37] Mintchev, S., Shintake, J., and Floreano, D., 2018, "Bioinspired Dual-Stiffness Origami," Sci. Rob., **3**(20), p. eaau0275.
[38] Boyvat, M., Koh, J.-S., and Wood, R. J., 2017, "Addressable Wireless Actuation for Multijoint Folding Robots and Devices," Sci. Rob., **2**(8), p. eaan1544.
[39] Kim, S.-J., Lee, D.-Y., Jung, G.-P., and Cho, K.-J., 2018, "An Origami-Inspired, Self-Locking Robotic Arm That Can Be Folded Flat," Sci. Rob., **3**(16), p. eaar2915.
[40] Miyashita, S., Guitron, S., Ludersdorfer, M., Sung, C. R., and Rus, D., 2015, "An Untethered Miniature Origami Robot That Self-Folds, Walks, Swims, and Degrades," 2015 IEEE International Conference on Robotics and Automation (ICRA), Seattle, WA, May 26–30, IEEE, pp. 1490–1496.
[41] Butler, J., Bowen, L., Wilcox, E., Shrager, A., Frecker, M. I., Von Lockette, P., Simpson, T. W., Lang, R. J., Howell, L. L., and Magleby, S. P., 2018, "A Model for Multi-Input Mechanical Advantage in Origami-Based Mechanisms," ASME J. Mech. Rob., **10**(6), p. 061007.
[42] Morgan, J., Magleby, S. P., and Howell, L. L., 2016, "An Approach to Designing Origami-Adapted Aerospace Mechanisms," ASME J. Mech. Des., **138**(5), p. 052301.
[43] Banerjee, H., Kai Li, T., Ponraj, G., Senthil Kumar, K., Lim, C. M., and Ren, H., 2019, "Origami-Layer-Jamming Deployable Retractor With Variable Stiffness and Tactile Sensing," ASME J. Mech. Rob., pp. 1–15.

[44] Howell, L. L., 2001, *Compliant Mechanisms*, John Wiley & Sons, New York.
[45] Dearden, J., Grames, C., Orr, J., Jensen, B. D., Magleby, S. P., and Howell, L. L., 2018, "Cylindrical Cross-Axis Flexural Pivots," Precision Eng., **51**, pp. 604–613.
[46] Grames, C. L., Tanner, J. D., Jensen, B. D., Magleby, S. P., Steger, J. R., and Howell, L. L., 2015, "A Meso-Scale Rolling-Contact Gripping Mechanism for Robotic Surgery," ASME 2015 International Design Engineering Technical Conferences and Computers and Information in Engineering Conference, Boston, MA, Aug. 2–5, American Society of Mechanical Engineers, p. V05AT08A034.
[47] Liu, J., Hall, B., Frecker, M., and Reutzel, E. W., 2013, "Compliant Articulation Structure Using Superelastic Nitinol," Smart Mater. Struct., **22**(9), p. 094018.
[48] Guest, S., and Pellegrino, S., 1994, "The Folding of Triangulated Cylinders, Part I: Geometric Considerations," ASME J. Appl. Mech., **61**(4), pp. 773–777.
[49] Guest, S., and Pellegrino, S., 1994, "The Folding of Triangulated Cylinders, Part II: The Folding Process," ASME J. Appl. Mech., **61**(4), pp. 778–783.
[50] Guest, S., and Pellegrino, S., 1996, "The Folding of Triangulated Cylinders, Part III: Experiments," ASME J. Appl. Mech., **63**(1), pp. 77–83.
[51] Kresling, B., Abel, J. F., and Cooke, R. J., 2008, "Natural Twist Buckling in Shells: From the Hawkmoth's Bellows to the Deployable Kresling-Pattern and Cylindrical Miura-Ori," Proceedings of the 6th International Conference on Computation of Shell and Spatial Structures, Ithaca, NY, May 28–31.
[52] Wilson, L., Pellegrino, S., and Danner, R., 2013, "Origami Sunshield Concepts for Space Telescopes," AIAA Paper 2013-1594.
[53] Butler, J., Morgan, J., Pehrson, N., Tolman, K., Bateman, T., Magleby, S. P., and Howell, L. L., 2016, "Highly Compressible Origami Bellows for Harsh Environments," ASME 2016 International Design Engineering Technical Conferences and Computers and Information in Engineering Conference, Charlotte, NC, Aug. 21–24.
[54] Butler, J., Magleby, S., Howell, L., Mancini, S., and Parness, A., 2017, "Highly Compressible Origami Bellows for Microgravity Drilling-Debris Containment," AIAA SPACE and Astronautics Forum and Exposition, Orlando, FL, Sept. 12–14, p. 5341.
[55] Cai, J., Deng, X., Zhou, Y., Feng, J., and Tu, Y., 2015, "Bistable Behavior of the Cylindrical Origami Structure With Kresling Pattern," ASME J. Mech. Des., **137**(6), p. 061406.
[56] Yasuda, H., Lee, M., and Yang, J., 2016, "Tunable Static and Dynamic Behavior of Triangulated Cylindrical Origami," Proceedings of the IASS Annual Symposium 2016, Tokyo, Japan, Sept. 26–30.
[57] Cai, J., Liu, Y., Ma, R., Feng, J., and Zhou, Y., 2017, "Nonrigidly Foldability Analysis of Kresling Cylindrical Origami," ASME J. Mech. Rob., **9**(4), p. 041018.
[58] Cai, J., Deng, X., Zhang, Y., Feng, J., and Zhou, Y., 2016, "Folding Behavior of a Foldable Prismatic Mast With Kresling Origami Pattern," ASME J. Mech. Rob., **8**(3), p. 031004.
[59] Herron, J. D., 2018, "Augmented Design Capabilities for Origami Tessellations," MS thesis, Brigham Young University, Provo, UT.
[60] Sargent, B., Brown, N., Jensen, B. D., Magleby, S. P., Pitt, W. G., and Howell, L. L., 2019, "Heat Set Creases in Polyethylene Terephthalate (PET) Sheets to Enable Origami-Based Applications," Smart Mater. Struct., **28**(11), p. 115047.